IEEE Open Journal of the
Solid-State Circuits Society

Received 14 July 2021; revised 4 October 2021; accepted 10 October 2021. Date of publication 15 October 2021;
date of current version 10 December 2021.

Digital Object Identifier 10.1109/OJSSCS.2021.3120238

A Review of Semiconductor-Based Monolithic Optical Phased Array Architectures

HOSSEIN HASHEMI (Fellow, IEEE)

Department of Electrical and Computer Engineering, University of Southern California, Los Angeles, CA 90272, USA

CORRESPONDING AUTHOR: H. HASHEMI (e-mail: hosseinh@usc.edu)

This work was supported in part by Tower Semiconductor; in part by Samsung; in part by Toyota Central R&D Corporation;
and in part by the USC Pratt & Whitney Institute for Collaborative Engineering (PWICE).

ABSTRACT Semiconductor-based monolithic optical phased arrays (OPA) enable optical beam-steering for lidar and 3D imaging, free-space optical communications, projection and 3D holographical displays, and neural probes among many other possible applications. This paper provides a review of OPA operating principles, architectures, key building blocks, and remaining research challenges.

INDEX TERMS Free space optical communications, holography, lidar, phased arrays, photonic integrated circuits, silicon photonics.

I. INTRODUCTION

IN HIS December 11, 1909 Nobel Lecture, Karl Ferdinand Braun stated [1] "It had always seemed most desirable to me to transmit the waves, in the main, in one direction only." He then went on to explain how an array of three antennas, when connected to a signal source with appropriate delays, can create a directional transmitter. In 1940s, researchers in MIT's newly established Radiation Laboratory that included another Nobel Laureate by the name of Luis Walter Alvarez demonstrated the first microwave phased array radar. In the following decades, electronic steering of radiofrequency waves was utilized primarily in realization of airborne and ground-based radars. In his seminal 1965 paper [2], Gordon Moore while predicting the exponential increase of transistor count on a single chip also prophesized that successful realization of monolithic phased arrays "could completely revolutionize radar". In subsequent years, monolithic microwave integrated circuits (MMICs) gradually replaced bulky microwave components in large-scale phased arrays. Later advancements in silicon and CMOS radiofrequency integrated circuits (RFIC) led to monolithic realization of phased array transceivers. Today, monolithic phased array transceivers are in high-volume production for 5G wireless communication devices and automotive radars.

Shortly after the invention of laser in 1960, phased array schemes that enable electronic steering of laser beam for projection TV display, optical radar, free-space optical communications, and high-speed printing systems were proposed [3], [4]. However, the difficulty to accurately control the relative phases of an optical signal that are emitted from wavelength-spaced apertures prohibited realization of optical phased arrays for decades. In the meanwhile, optical beam-steering was achieved primarily through mechanical means such as rotating mirrors, and to a lesser degree non-mechanically through liquid crystal optical structures whose transmissive or reflective properties depend on the application of a voltage.

In the 1980s, advancements in materials growth and fabrication technology led to the monolithic realization of key photonic and electro-optical components such as distributed feedback (DFB) and distributed Bragg reflector (DBR) lasers, detectors, high-quality-factor resonators, modulators, and arrays of components and sub-systems. The continued advancements in the 1990s led to realizations of semiconductor photonic integrated circuits (PIC) primarily for optical communication applications. While most implementations were based on group III-V compound semiconductors, researchers started to investigate realization of photonic devices on a silicon substrate alongside electronic components with an ultimate objective of creating complex silicon electro-optic integrated circuits. Since the 2000s, there has been a rapid growth of silicon photonics (SiP)

research leading to commercial realization of complex silicon opto-electronic transceivers [33], [34].

Over the past decade, several monolithic optical phased arrays (OPA) with various complexities have been reported [6]–[30]. Silicon platform has been the technology of choice for such implementations due to the ability to realize complex electro-optical integrated systems monolithically on a single compact chip at low cost. Given that most silicon photonic processes have been optimized for the 1310 nm and 1550 nm wavelength for fiber-optical communication applications, most of the implemented optical phased arrays have been designed to operate the same wavelength. The major envisioned applications for these OPAs are lidar and free-space optical communications. There is a recent interest in optical phased arrays that work in the visible wavelengths for 3D holographic displays and biomedical applications. This article covers the fundamentals and selected developments in the areas of semiconductor-based monolithic optical phased arrays. It is emphasized that creating and steering a single optical beam, while an important application enabler, is only a special case of what a generic OPA can do. Section II provides a concise review of the phased array operating principle. Section III covers various architectures of optical phased arrays. Section IV covers the effect of mismatches in the array and on-chip calibration methods. Section V summarizes the technology, key building blocks, and implementation challenges associated with realization of OPAs. Section VI concludes the paper and highlights selected remaining research challenges related to OPAs.

II. PHASED ARRAYS

A. BASIC PRINCIPLE

Interference is a key feature of waves and is fundamentally a result of coherent superposition of complex-valued wave functions. The phase of propagating sinusoidal wave changes linearly with propagation distance. When multiple equifrequency sinusoidal propagating waves reach the same point, they will combine constructively or destructively depending on their relative phases.

In a phased array transmitter, interference is caused by electromagnetic waves that are emitted by multiple antenna elements. Consider a modulated signal of the form $X_{TX}(t) = s(t)e^{j\omega_o t}$ that feeds multiple transmission antennas where $s(t)$ is the complex information signal and ω_o is the carrier frequency (Fig. 1). These propagating waves, once reaching the same point in space,[1] result in a signal given by

$$X_{RX}(t) = \frac{\sum_{n=1}^{N} a_n X_{TX}(t-\tau_n)}{\sqrt{N}}, \tag{1}$$

where N is the number of transmitting antennas, and a_i and τ_i represent the attenuation level and delay that the transmitted signal faces as it propagates from the n^{th} antenna to the target point.

1. Assume only line-of-sight between the transmitting antennas and the target point (receiver).

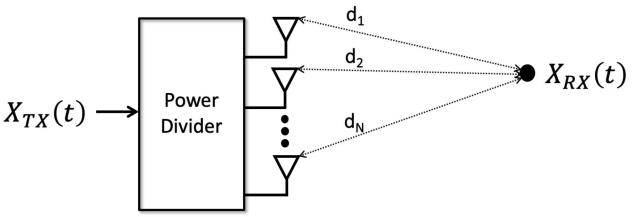

FIGURE 1. Free-space interference of electromagnetic waves.

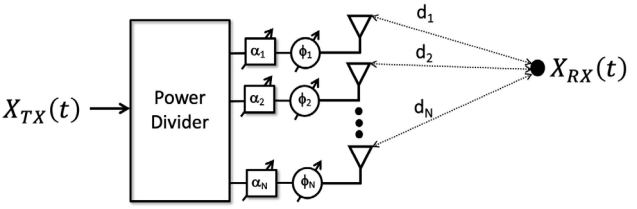

FIGURE 2. Beamforming.

Assuming similar attenuation levels and narrowband modulation,[2] the received signal strength at any given point can be expressed as

$$X_{RX}(t) = as(t-\tau)e^{j\omega_o t}\frac{\sum_{n=1}^{N} e^{-j2\pi\frac{d_n}{\lambda}}}{\sqrt{N}}, \tag{2}$$

where $d_n = \tau_n \times c$ is the distance from the n^{th} antenna to the target point, c is the speed of light, and $\lambda = 2\pi c/\omega_o$ is the wavelength. The summation in the above expression creates the interference pattern. In a fixed geometry of transmitting antennas, the interference pattern can be controlled by adjusting the relative amplitudes α_n and phases φ_n of radiating signals as

$$\begin{aligned} X_{RX}(t) &= as(t-\tau)e^{j\omega_o t}\frac{\sum_{n=1}^{N} \alpha_n e^{-j\left(2\pi\frac{d_n}{\lambda}-\varphi_n\right)}}{\sqrt{N}} \\ &= as(t-\tau)e^{j\omega_o t}\frac{\sum_{n=1}^{N} c_n e^{-j2\pi\frac{d_n}{\lambda}}}{\sqrt{N}}, \end{aligned} \tag{3}$$

where $c_n = \alpha_n e^{j\varphi_n}$ is a complex coefficient.

The controllable interference pattern, created by the summation in the above expression, is also referred to as *antenna array pattern* or *beamforming pattern*. The desired interference pattern can be formed close to or far from the transmitting antennas in the so-called *near-field beamforming* [35] or *far-field beamforming* schemes, respectively. The constructive (in-phase) and destructive (out-of-phase) interference of waves results in peaks and nulls in the array pattern. The peaks in the array pattern may be adjusted to maximize the signal strength transmitted to or received from specific desired locations. For instance, in phased array radars, the peaks in the array pattern are dynamically adjusted to search and track the desired targets. The

2. The modulation bandwidth should be smaller than the inverse of the maximum propagation delay difference corresponding to different transmitting antennas.

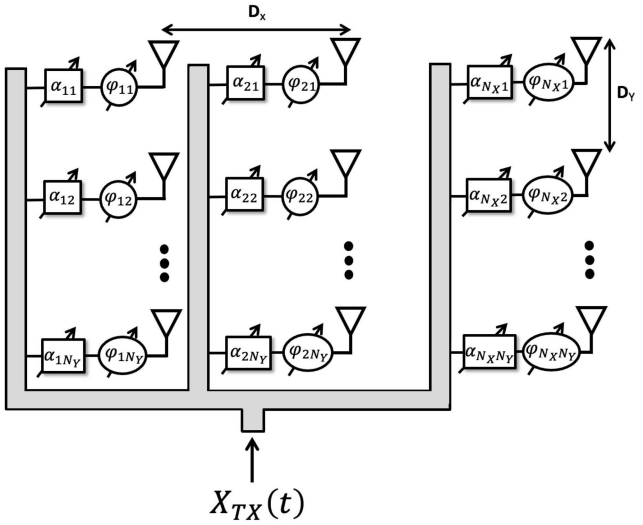

FIGURE 3. 2D beamforming with uniform antenna spacing.

nulls in the array pattern can be adjusted to minimize the interference from/to unwanted locations. Reciprocity implies that the transmitting antenna array patterns are the same for receiving antenna arrays.

B. SPECIAL CASE: UNIFORM 2D ARRAYS

Consider a special case where antennas are placed on an $N_X \times N_Y$ grid with a uniform spacing D_X and D_Y in the two dimensions. The interference pattern can be represented as

$$X_{RX}(t) = as(t-\tau)e^{j\omega_o t}\frac{\sum_{m=1}^{N_Y}\sum_{n=1}^{N_X} c_{nm}e^{-j2\pi\frac{d_{nm}}{\lambda}}}{\sqrt{N_X N_Y}}, \quad (4)$$

where $c_{nm} = \alpha_{nm}e^{j\varphi_{nm}}$ is a complex number, and α_{nm} and φ_{nm} represent the relative amplitude and phase of signal that is fed to the *(n,m)* radiator, and d_{nm} is the distance from the *(n,m)* radiator to the target point. In the far-field ($d_{nm} \gg N_X D_X$ & $N_Y D_Y$), this expression would simply to

$$X_{RX}(t) = as(t-\tau)e^{j\omega_o(t-\tau)} \frac{\sum_{m=1}^{N_Y}\sum_{n=1}^{N_X} c_{nm}e^{-j2\pi\frac{nD_X\sin\theta_X + mD_Y\sin\theta_Y}{\lambda}}}{\sqrt{N_X N_Y}}, \quad (5)$$

where θ_X and θ_Y are angle from the array to the target point relative to the array's normal plane in the X and Y dimensions. The 2D beamforming summation, also referred to as the array factor (AF), resembles the form of a 2D Fourier transform as

$$AF(\theta_X,\theta_Y) = \frac{\sum_{m=1}^{N_Y}\sum_{n=1}^{N_X} c_{nm}e^{-j2\pi\frac{nD_X\sin\theta_X + mD_Y\sin\theta_Y}{\lambda}}}{\sqrt{N_X N_Y}} = \frac{\sum_{m=1}^{N_Y}\sum_{n=1}^{N_X} c_{nm}e^{-j\frac{2\pi}{N_X}n\Omega_X}e^{-j\frac{2\pi}{N_Y}n\Omega_Y}}{\sqrt{N_X N_Y}}, \quad (6)$$

where $\Omega_X = \frac{N_X D_X \sin\theta_X}{\lambda}$ and $\Omega_Y = \frac{N_Y D_Y \sin\theta_Y}{\lambda}$.

The following general results hold for uniform arrays.

1. In general, complex coefficients $c_{nm} = \alpha_{nm}e^{j\varphi_{nm}}$ can be found through an inverse Fourier transform for a desired array factor $AF(\theta_X,\theta_Y)$.

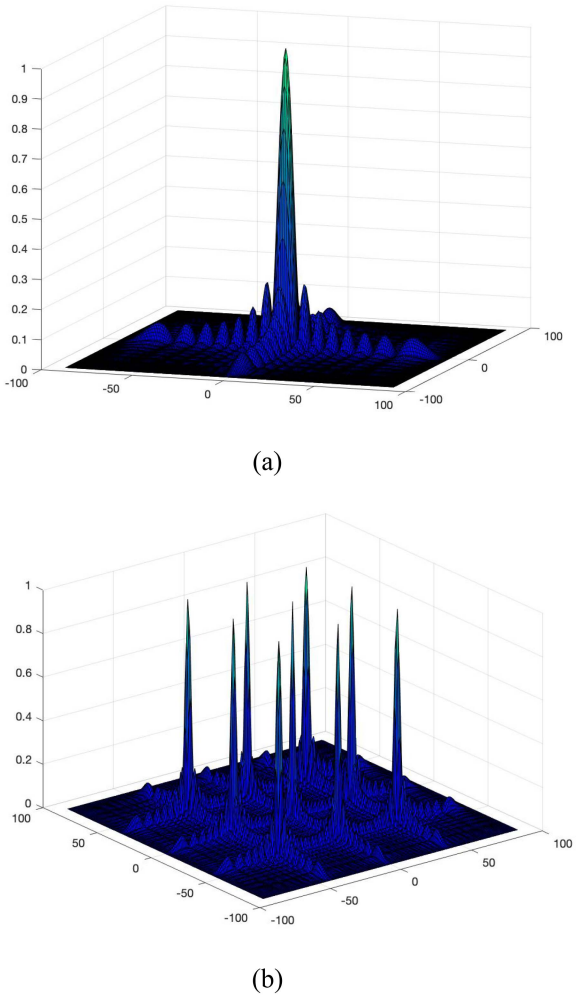

FIGURE 4. 16 x 16 element 2D array patterns: (a) $D_X = D_Y = \lambda/2$, (b) $D_X = D_Y = 3\lambda/2$.

2. In a special case, the array factor $AF(\theta_X,\theta_Y)$ has a main peak whose direction can be adjusted through complex coefficients $c_{nm} = \alpha_{nm}e^{j\varphi_{nm}}$ (Fig. 4a). In fact, it is easy to show that by merely adjusting the phases of complex coefficients to have linear progression along the X and Y axes as $c_{nm} = e^{j(n\Delta_X + m\Delta_Y)}$, a single beam is created that points at a spatial angle depending on phase constants Δ_X and Δ_Y. However, amplitudes α_{nm} offer additional degrees of freedom that can be used, for instance, to control the array factor at all angles and increase the side mode suppression ratio (SMSR).

3. If D_X or D_Y is greater than $\lambda/2$, the array pattern will have the same value for some image angles. For instance, if $D_X > \lambda/2$ and the c_{nm} coefficients are set to create a single beam pointing at a given angle, θ_{X0}, the array will create at least one more beam pointing at another angle, $\theta_{Xi} = \sin^{-1}(\lambda/2D_X)$ (Fig. 4b). These additional unwanted beams are referred to as grating lobes.[3]

3. To achieve grating-lobe-free arrays, two approaches can be taken: (a) uniform array with < mathrm$\lambda/2$ spacing, (b) nonuniform array.

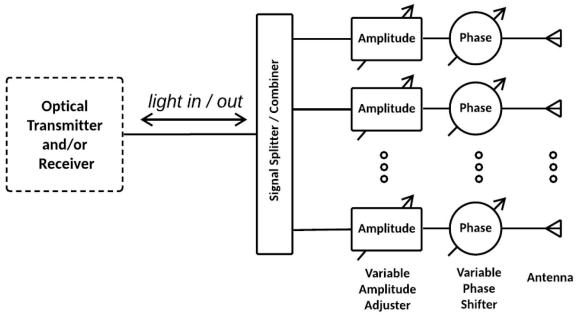

FIGURE 5. Generic phased array with signal-path beamforming.

4. The minimum full width at half maximum (FWHM) of the main beam in the two dimensions is inversely proportional to the array size $N_X D_X$ and $N_Y D_Y$, respectively.

5. The distances between adjacent antennas in a phased array need not be equal. In a so-called nonuniform or aperiodic array, the locations of the antennas can be optimized to achieve a desired FWHM for the main beam, grating-lobe-free FOV, and SMSR [5].

III. OPTICAL PHASED ARRAY ARCHITECTURES

A. SIGNAL-PATH BEAMFORMING

In the most general approach, phase shifting, amplitude adjustment, and combining all occur directly on the transmitted or received optical signals. Figure 5 shows schematic of such a phased array, with a so-called signal-path beamforming, consisting of an array of antennas each connected to a variable phase shifter and a variable amplitude adjuster. In some implementations, variable amplitude adjusters may be omitted at the expense of reduced beamforming flexibility. The structure of Figure 1 may be used either as a phased array transmitter or a phased array receiver. In fact, if the variable phase shifter and the variable amplitude adjuster are bidirectional, the structure may be used as a phased array transceiver. The antennas may be placed on a line (linear or 1D array) [11]–[23] or on a plane (2D array) [6]–[9] with uniform or nonuniform spacing.

Two-Dimensional (2D) Optical Phased Arrays: Figure 6 shows the schematic of a 2D OPA, in a signal-path beamforming architecture, where the variable phase shifters and variable amplitude adjusters are placed local to each antenna element. In the absence of gain elements, say in the current SiP foundry offerings, variable amplitude adjusters may be realized as variable attenuators. Variable attenuators are bidirectional and enable transmit and receive functions using the same phased array signal-path beamformer. Couplers with appropriate coupling lengths are used to ensure even optical power distribution across the array. The multi-wavelength size of the antennas, variable phase shifters, and variable amplitude adjusters determine the minimum spacing between adjacent antenna elements to be several wavelengths. Therefore, the unambiguous field-of-view (FOV) – FOV without additional grating lobes – of such implementations is quite limited [6], [7].

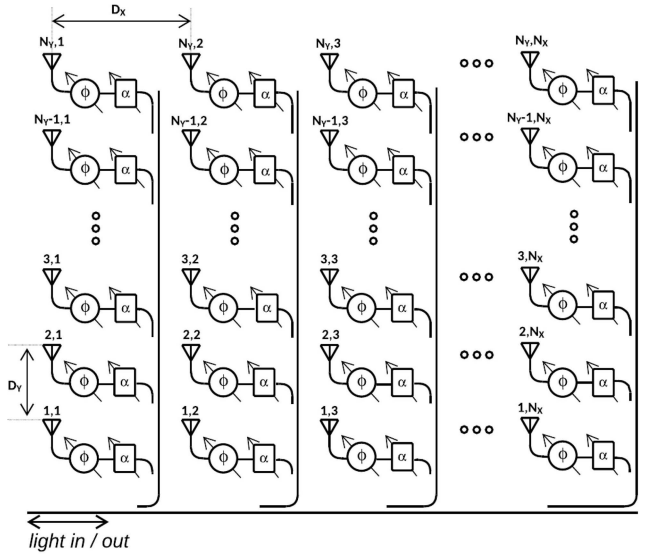

FIGURE 6. 2D OPA with local amplitude and phase control per antenna in a signal-path beamforming scheme.

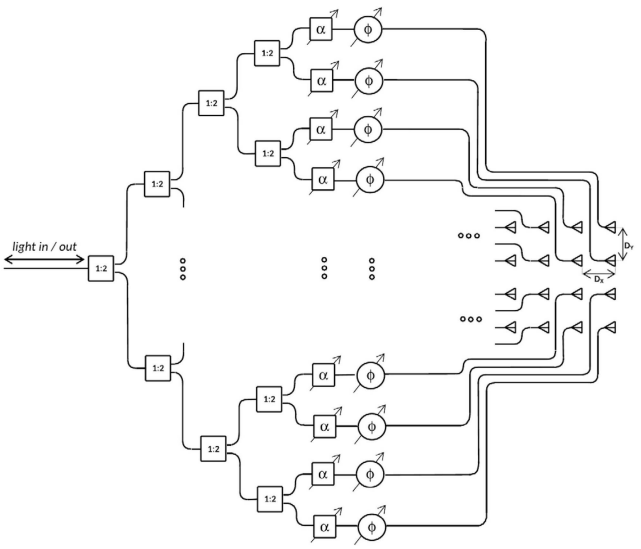

FIGURE 7. 2D OPA with remote variable phase shifters and amplitude adjusters in a signal-path beamforming scheme.

To reduce the spacing between adjacent antennas, the variable phase shifters and amplitude adjusters may be placed at a distance from the 2D antenna array in a signal-path beamforming scheme [8] (Figure 7). Any signal splitting (combining) scheme, including the binary tree structure of Fig. 3 using 1:2 power splitters/combiners, may be used at the transmitting (receiving) array input (output). In a small-scale array, such as the 4 x 4 array of Fig. 7, routing the optical signals from the remote variable phase and amplitude adjusters to the 2D antenna array elements with close spacing is possible. However, as the array size increases, routing $N_X \times N_Y$ optical waveguides to the 2D antenna array requires increasing the distance between the antennas.

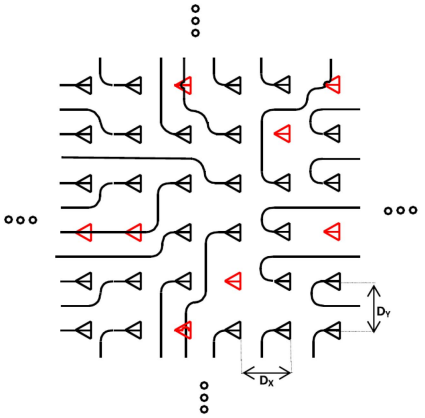

FIGURE 8. Sparse 2D OPA (antennas shown in red are not present) where optical waveguides route signals from the sparse array to remote variable phase shifters and amplitude adjusters.

TABLE 1. Performance specifications of monolithic 2D optical phased arrays in a signal-path beamforming scheme.

	Caltech (2019) [9]	Caltech (2015) [8]	USC (2015) [7]	MIT (2013) [6]
Wavelength (λ)	1550 nm	1550 nm	1550 nm	1550 nm
Array Size	128 (2D sparse)	4 x 4	8 x 8	8 x 8
Antenna Spacing	3.6 λ (minimum spacing)	32 λ	21.3 λ	5.8 λ
Grating-Lobe Free Steering Angle (FOV)	±8°	±0.9°	±0.8°	±5°
FWHM for Main Beam	0.8°	0.5°	0.45°	1.1°
Side Mode Suppression Ratio (SMSR)	12 dB	6 dB	12 dB	N/A
Power Consumption per Element	10.6 mW	N/R	21 mW	9 mW
Integrated Electronics	Yes	No	Yes	No
Phase Control Mechanism	Thermo-Optic	Carrier Injection	Thermo-Optic	Thermo-Optic
Intensity Control Mechanism	N/A	N/A	Thermo-Optic	N/A
Technology	Si PIC + 65nm CMOS	Si PIC	180nm RF SOI CMOS	Si PIC

In a 2D optical phased array in a signal-path beamforming scheme with remote variable phase shifters and amplitude adjusters, the array size may be increased without a significant increase in the antenna spacing by judiciously removing some of the antennas in a uniform 2D grid [9] (Fig. 8). In such a so-called sparse array, the FWHM of the main beam and the appearance of grating lobes are still functions of the total array size and antenna spacing, respectively, while the SMSR is worse than that of a complete array.

Table 1 summarizes the performance of selected reported semiconductor-based 2D optical phased arrays in a signal-path beamforming scheme. It is seen that even with sparse arrays, the grating-lobe-free steering angle or FOV is quite limited. Semiconductor-based monolithic large-scale 2D optical phased array with acceptable grating-lobe-free steering angle or FOV, FWHM of the main beam, and SMSR is still an open research problem.

One-Dimensional (1D) Optical Phased Arrays: The implementation of large-scale 1D OPAs with small antenna spacing is straightforward as the variable phase shifters and amplitude adjusters may be placed far from each other and from the antenna array (Fig. 9). In fact, monolithic optical phased arrays with half-wavelength antenna spacings have been demonstrated [10]. In arrays with closely spaced antennas, unwanted coupling between adjacent antennas or

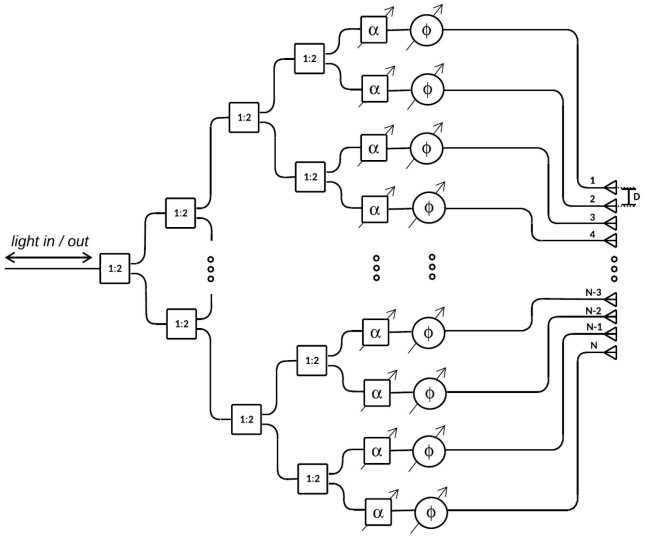

FIGURE 9. 1D OPA in a signal-path beamforming scheme.

waveguides should be reduced, for instance, by dispersion engineering [10].

Naturally, 1D phased arrays can only form and control the spatial beam in one dimension. In certain applications, such as in a scanning LiDAR, the objective is to form and steer a single narrow beam in two dimensions. The phased array principle may be used to steer the beam in one dimension (phased array beam steering), and the dependency of radiation angle off the grating couplers acting as optical antennas is used to steer the beam in the other dimension (wavelength beam steering) [11].

Over the past decade, several optical phased arrays with different complexity levels have been reported (Table 2). A few different approaches have been used to reduce the number of optical variable phase shifters and/or the number of associated electronic drivers (Table 3). The downside with such approaches is the reduced degrees of freedom over forming beam patterns, and possibly more sensitivity to process mismatches.

B. LO-PATH BEAMFORMING

In the most general communication or active imaging scheme, the information is embedded in the amplitude and phase of the optical field as

$$E(t) = E_o(t)\cos(\Omega t + \emptyset(t)), \tag{7}$$

where Ω is the optical carrier frequency, and $E_o(t)$ and $\emptyset$(t) are the amplitude modulation (AM) and the phase modulation (PM) information components, respectively. Coherent detection leads to better signal to noise ratio (SNR) in the case of amplitude modulation and is necessary in the case of phase modulation. The basic idea of coherent detection (coherent receiver) is to remove the carrier term leaving only the information content.

This is mathematically achieved by multiplying the received signal with the in-phase and quadrature phases

TABLE 2. Performance specifications of monolithic 1D optical phased arrays in a signal-path beamforming scheme.

	USC (2021) [20]	Analog Photonics (2018) [19]	UCD/LMC (2019) [18]	Berkeley/MIT (2019) [17]	Analog Photonics (2018) [16]	Columbia (2018) [15]	Columbia (2018) [10]	Intel (2016) [14]	UCSB (2015) [13]	UT Austin (2014) [12]	UCSB (2011) [11]
Wavelength (l)	1550 nm	1550 nm	1550 nm	1550 nm	1550 nm	1550 nm	1550 nm	1310 nm	1550 nm	1550 nm	1550 nm
Array Size	256	8192	24	32	512	512	64	128	32	16	16
Antenna Spacing	0.9 λ	0.64 λ	0.84 λ	2.6 λ	1.06 λ	0.84 λ	0.5 λ	Nonuniform (avg = 5.5 λ)	2.6 λ	2.6 λ	2.9 λ
Grating-Lobe Free Steering Angle (FOV_f)	±33.5°	±50°	±33°	±8°	±28°	±35°	±60°	±40°	±11.5°	±10°	±10°
FWHM Beam Spot Size (f x q)	0.32° x 0.95°	0.01° x 0.039°	NR x NR	0.6° X 0.15°	0.04° x 0.04°	0.15° x 0.15°	1.2° x NR	0.14°x 0.14°	1° x 0.6°	1.2° x 0.5°	0.6° x 1.6°
Side Mode Suppression Ratio (SMSR)	NR	10 dB	7 dB	8.5 dB	12 dB	13 dB	11.4	9 dB	6 dB	10 dB	10 dB
Power Consumption per Element	5.2 mW	0.3 mW (PIC + EIC)	24 mW	40 mW	4 mW	5.2 mW	10 mW	80 mW	160 mW	40 mW	430 mW
Integrated Electronics	Yes	Yes (flip-chip IC)	No	Yes	No	No	No	No	No	No	No
Phase Control Mechanism	Thermo-Optic	Electro-Optic	Thermo-Optic	Thermo-Optic	Electro-Optic	Thermo-Optic	Thermo-Optic	Thermo-Optic	Electro-Optic	Thermo-Optic	Thermo-Optic
Intensity Control Mechanism	Thermo-Optic (@ Subarrays)	NA	NA	NA	NA	NA	NA	NA	Optical Gain	NA	NA
Wavelength Beam Steering Angle (FOV_q) (Required Wavelength Change)	16° (100 nm)	17° (120 nm)	3.3° (20 nm)	18.5° (120 nm)	15° (NR)	14° (45 nm)	NR	17° (100 nm)	3.6° (34.5 nm)	15° (100 nm)	14° (100 nm)
Technology	Si PIC + 180nm CMOS	Si PIC + Flip Chipped CMOS IC	Si PIC	Si PIC + 65nm CMOS	Si PIC Co-Packaged with III-V Laser	Si PIC	Si PIC	Si PIC	Hybrid GaAs/Si with Tunable Laser	Si PIC	Si PIC

TABLE 3. Performance specifications of monolithic 1D optical phased arrays in a signal-path beamforming scheme with reduced number of variable optical phase shifters or associated electronic drivers.

	USC (2017) [23]	MIT (2016) [22]	Ghent/EPFL (2009) [21]
Wavelength (λ)	1550 nm	1550 nm	1550 nm
Array Size	1024	50	16
Antenna Spacing	1.3 λ	1.3 λ	1.87 λ
Grating-Lobe Free Steering Angle (FOV_ϕ)	±22.5°	±23°	±1.15°
FWHM Beam Spot Size (ϕ x θ)	0.03° x NR	0.85° x 0.18°	2.7° x 2.5°
Side Mode Suppression Ratio (SMSR)	9 dB	9 dB	NR
Power Consumption per Element	54 mW	12 mW	16.4 mW
Integrated Electronics	Yes	No	No
Phase Control Mechanism	Thermo-Optic	Thermo-Optic	Thermo-Optic
Intensity Control Mechanism	Thermo-Optic (Partial)	NA	NA
Wavelength Beam Steering Angle (FOV_θ) (Required Wavelength Change)	NR	36° (187 nm)	14.1° (100 nm)
Technology	180nm SOI RF CMOS	Si PIC	Si PIC
Architecture (to reduce the number or complexity of variable phase shifters)	Hierarchical Subarrays with Common Phase Control	Grouped Canscaded Phase Shifters	Linearly Increasing Phase Shifters Across the Array

of the unmodulated carrier signal, also known as local oscillator (LO) as

$$\begin{cases} I(t) = E(t) \times E_{LO}\cos(\Omega t) \ = E_{LO}E_o(t)\cos(\emptyset(t)) \\ Q(t) = E(t) \times E_{LO}\sin(\Omega t) \ = E_{LO}E_o(t)\sin(\emptyset(t)), \end{cases} \quad (8)$$

The above set of equations easily result in the AM term $E_o(t) = \sqrt{I^2(t) + Q^2(t)}/E_{LO}$ and the PM term $\emptyset(t) = \tan^{-1}(Q(t)/I(t))$.

This mathematical operation, in optical domain, is often achieved by adding the modulated waveform E_o by the in-phase and quadrature phases of the LO signal and passing the combined signal into photodetectors. The second-order nonlinearity of the photodiodes result in the multiplication function as

$$\begin{cases} I_{PD,I}(t) = R_{PD}\overline{[E(t) + E_{LO}\cos(\Omega t)\ ]^2} \\ \quad = R_{PD}\left(\frac{E_o(t)^2}{2} + \frac{E_{LO}{}^2}{2} + E_{LO}E_o(t)\cos(\emptyset(t))\ \right) \\ I_{PD,Q}(t) = R_{PD}\overline{[E(t) + E_{LO}\sin(\Omega t)\ ]^2} \\ \quad = R_{PD}\left(\frac{E_o(t)^2}{2} + \frac{E_{LO}{}^2}{2} + E_{LO}E_o(t)\sin(\emptyset(t))\ \right), \end{cases} \quad (9)$$

where R_{PD} is the responsivity of the photodiode, and all the other terms are naturally "filtered out" by the photodiode. The two unknowns, $E_o(t)$ and $\emptyset(t)$ may be derived from these set of equations. The DC term, $E_{LO}{}^2/2$, may also be removed in a balanced photodiode configuration. Alternatively, one can also directly apply the signal to another photodetector to extract $E_{LO}{}^2/2$ and subtract it from the Eqn. (9) resulting in a set of equations that resemble Eqn. (8) that can easily yield $E_o(t)$ and $\emptyset(t)$. The signal-to-noise ratio (SNR) in a coherent optical receiver is given by

$$\text{SNR} = \frac{P_o}{\left[\frac{q_e \times \varepsilon}{R_{PD}} + \frac{\varepsilon^2 \times P_{LO} \times RIN}{4} + \frac{2S_{I,TIA}}{P_{LO} \times R_{PD}{}^2}\right]BW}, \quad (10)$$

where P_o and P_{LO} are the power of the received signal and local oscillator, respectively, q_e is a unit electron charge, ε is the mismatch of the balanced photodetectors, RIN is the relative intensity source of the laser, $S_{I,TIA}$ is the input-referred current noise power spectral density of the transimpedance amplifier (TIA), and BW is the bandwidth. In the shot-noise limited case (only first term of denominator), the LO power does not affect the SNR. However, once the effects of laser RIN and TIA input-referred noise are included, there may be an optimum LO power that maximizes SNR.

The mathematical descriptions of Eqns. (8) and (9) sggest that, from the perspective of the receiver output, adding a constant phase term to $E(t)$ is equal to adding the complex conjugate of the same constant phase to the LO signal. This property can be used to realize optical phased array coherent receivers where the variable phase shifters are in the LO path (Fig. 10).

Assuming that the LO power in both schemes remains the same, the LO power and the signal power that reach each of the photodiodes in the LO-path beamforming scheme are N times smaller compared with those in the signal-path beamforming scheme (E_{LO} and $E_o(t)$ are smaller by $\sqrt{N}$). In the LO path beamforming scheme, the loss of variable phase shifters and signal combiners move from the signal path to the LO path. Therefore, from Eqn. (9), the photodiode output current remains the same in both beamforming schemes.

With more loss in the LO-path beamforming scheme, the LO power and hence the overall short noise (first term in

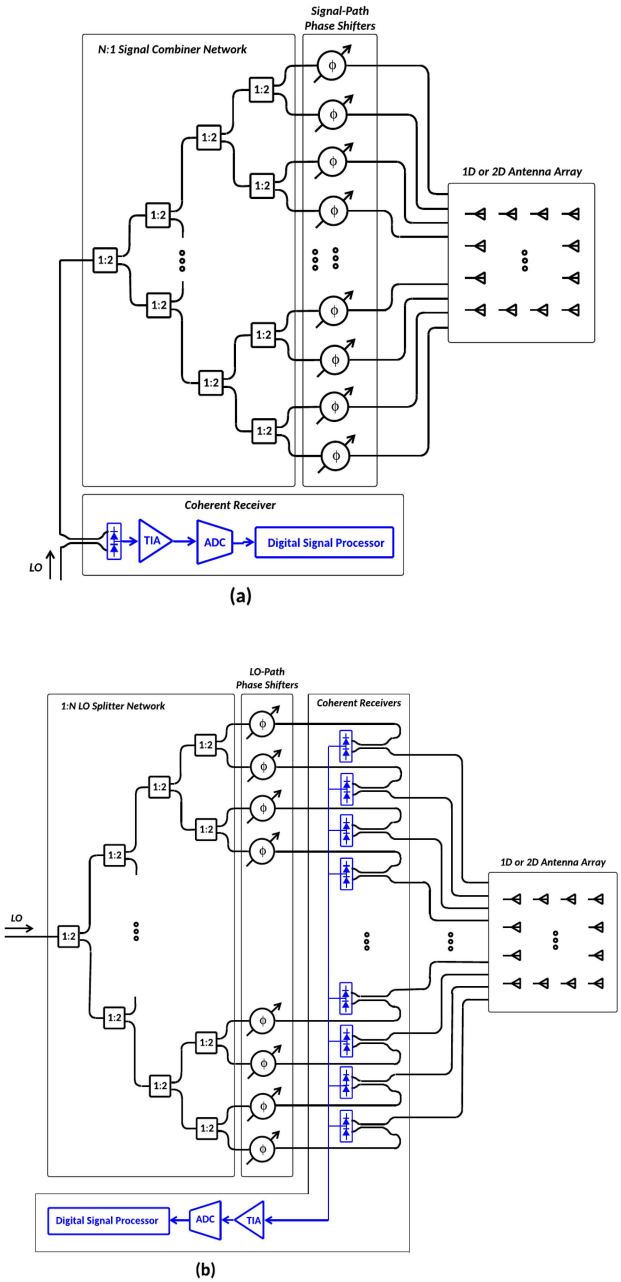

FIGURE 10. Coherent OPA receivers: (a) phased array in a signal-path beamforming scheme, (b) phased array in a LO-path beamforming scheme. Only one phase of I/Q is shown.

the denominator of Eqn. (10)) are smaller compared with those in the signal-path beamforming. Therefore, the LO-path beamforming may result in a higher shot-noise-limited signal-to-noise ratio (SNR) compared with the signal-path beamforming. As an example, [24] reports an 8 x 8 receiving array using the LO-path beamforming scheme capable of forming beams with FWHM of 0.75° over an 8° grating-lobe-free field of view.

C. ELECTRONIC-DOMAIN BEAMFORMING

In a coherent receiver, the phase shifting, amplitude adjustment, and subsequent signal combining may be performed in the electronic domain after the photodetection (Fig. 11). This approach leverages the advancements in analog, mixed-signal, and digital integrated circuits especially in light of transistor scaling. However, the large number of photonic-electronic interface signals necessitates tight monolithic or hybrid integration of photonics and electronics devices and circuits.

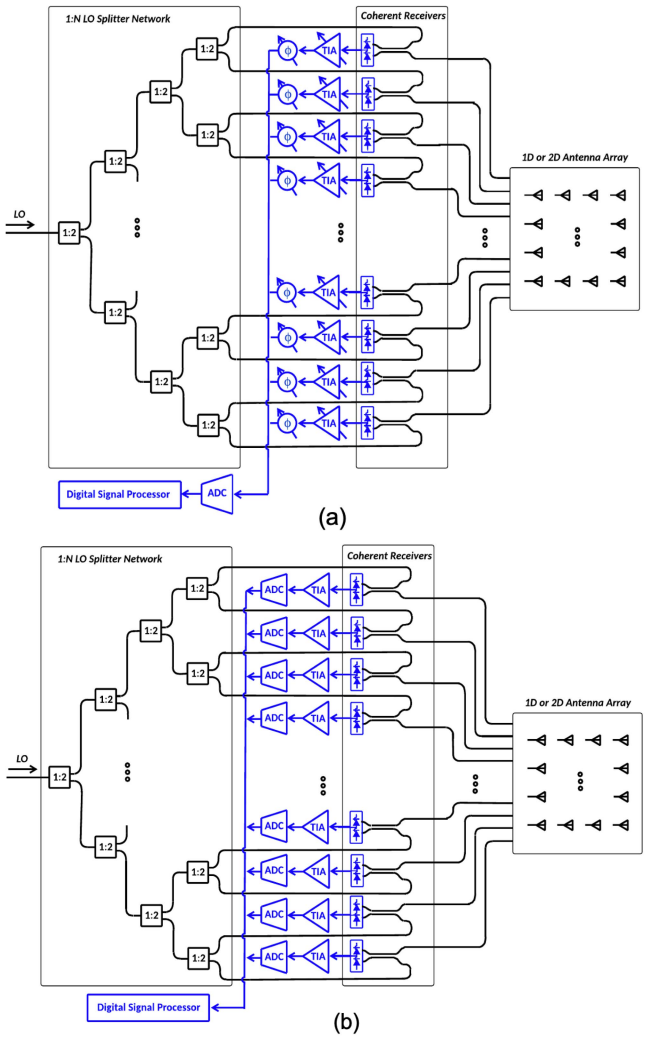

FIGURE 11. Coherent OPA receivers with electronic beamforming in (a) analog and (b) digital domains.

Depending on the desired antenna pitch, some or all of the photodetectors (PD), transimpedance amplifiers (TIA), analog phase shifters, and analog to digital converters (ADC) might be placed local to each optical antenna.

The digital beamforming array, in particular, is quite flexible as it allows for simultaneous detection of signals coming from different directions. To reduce the footprint and power consumption associated with the ADCs in a large-scale digital array, fewer time multiplexed ADCs may be used [25].

IV. ARRAY MISMATCHES AND ON-CHIP CALIBRATION

Phased arrays are quite sensitive to mismatches between the elements (e.g., seemingly identical variable phase shifters)

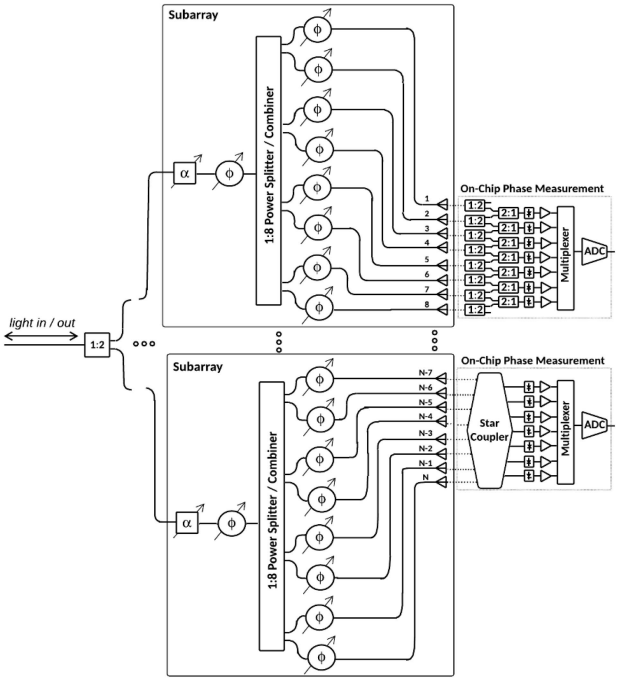

FIGURE 12. An N-element OPA in a signal-path beamforming scheme divided into 8-element subarrays. Two different on-chip optical phase measurement schemes, to facilitate array calibration in presence of process mismatches, are also shown.

as well as coupling between different signal paths. This problem is exacerbated in optical phased arrays where extremely small dimensional variations due to unavoidable process imperfection can lead to significant mismatches. For instance, the output optical phases of identical variable phase shifters with the same setting and driven by the same source may be quite different. Furthermore, compact realization of optical phased arrays naturally increases the unwanted optical and thermal coupling between adjacent components. Consequently, optical phased arrays require calibration – a process that can be extremely complicated and time consuming especially in the case of large-scale arrays with high-resolution control over variable phase shifters.

Optical phased arrays with independent variable amplitude adjusters per antenna can be calibrated easily by measuring the relative phase shift of two elements at the time (while the rest of paths are turned off using their variable amplitude adjusters) [7]. Incorporating independent variable amplitude adjusters per antenna may not be desirable in large-scale arrays as they lead to larger overall footprint and reduced overall power efficiency (either by introducing more optical loss in the case of variable attenuators or by consuming electrical power in the case of variable gain elements).

A large-scale phased array may be broken down to smaller subarrays in a hierarchical way where variable amplitude adjusters are introduced only at the boundaries of subarrays. Additional variable phase shifters may be added at these boundaries to offer additional degrees of freedom for array calibration and beamforming in presence of mismatches (Figure 12).

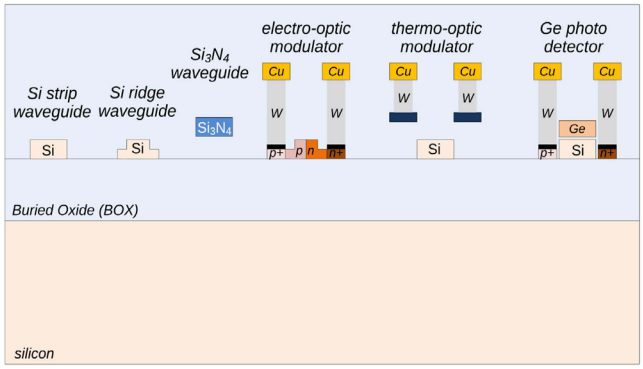

FIGURE 13. Cross-section of a generic silicon photonic process.

The effects of mismatches on the signals' relative phases across the array must be somehow measured and calibrated for prior to the array usage. Most current optical phased array implementations use benchtop optics and iterative algorithms to measure the far-field and/or near-field radiation patterns of a transmitting optical phased array to estimate and calibrate the phase mismatches. On-chip realization of mismatched phase measurements and calibration algorithms is an ongoing important research topic. The relative optical phases can be measured using an array of 1:2 splitters and 2:1 combiners, a planar lens [13], a star coupler [20], or a planar diffractor [26] that take a small fraction of unradiated optical signals, and feed them to photodetectors that are followed transimpedance amplifiers, an ADC, and a digital signal processor (DSP) that can calculate phase mismatches and adjust the control signals for the variable phase shifters in a feedback loop (Fig. 8).

Various calibration algorithms based on particle swarm optimization, hill climbing, gradient decent, stochastic gradient descent with objective functions such as maximizing the power of the main beam or the side mode suppression ratio have been reported [13], [14], [38].

V. IMPLEMENTATIONS

A. TECHNOLOGY

Optical phased arrays using the architectures discussed before may be implemented in various semiconductor technologies including silicon and III-V processes. For high-volume and cost-sensitive applications, there is a natural preference to use silicon photonic implementations. Figure 13 shows the cross section of a generic silicon photonic process showing key optical components. Some SiP processes include CMOS transistors whereas some standard bulk CMOS or SOI CMOS processes may be used to realize electronic-and-photonic integrated circuits (EPIC).

There are ongoing efforts towards heterogenous integration of III-V material into commercial SiP platforms to enable realization of semiconductor optical amplifiers (SOA) and lasers alongside the standard SiP components [36].

B. WAVEGUIDES

Silicon (Si) and silicon nitride (Si_3N_4) waveguides may be used to route the optical signal with a typical loss of around

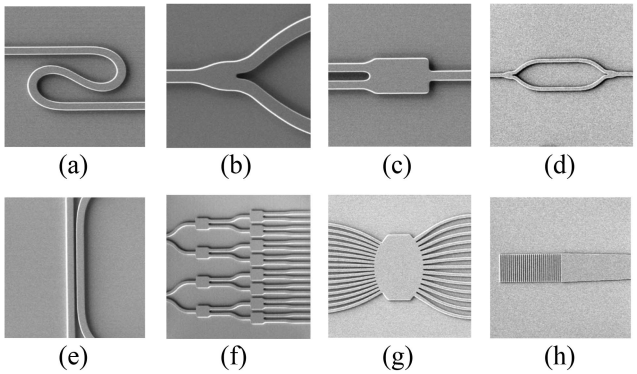

FIGURE 14. Representative silicon photonic passive components: (a) waveguide bend with Euler shape, (b) waveguide junction (1:2 power splitter), (c) multimode interferometer (1:2 power splitter), (d) Mach-Zehnder interferometer (MZI), (e) coupled waveguides, (f) binary tree power distribution network using 1:2 MMIs, (g) star coupler, (h) grating coupler (optical antenna).

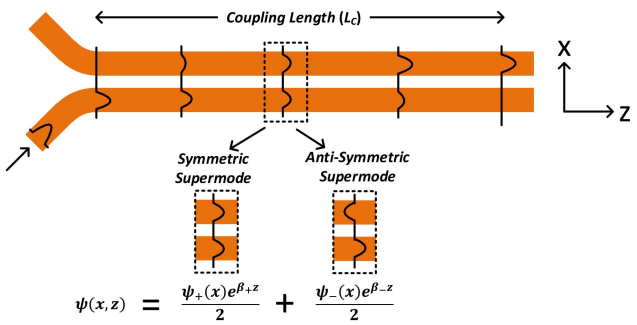

FIGURE 15. Coupled waveguides.

1 dB/cm for single-mode and less than 5 dB/m for multi-mode waveguides. Waveguides with smaller width support fewer propagating modes; however, they are more lossy due to low confinement and field scattering from the unsmooth waveguide sidewalls. On the other hand, wider waveguides have less loss due to higher confinement; but they can support multiple modes. One strategy might be using large widths for longer sections of waveguides to ensure low loss, and waveguide tapers to smaller widths prior to waveguide bends and other transitions, that can excite higher modes, to ensure single mode propagation. Compact routing requires tight waveguide bends. Noncircular optimized shapes may be used to realize compact low-loss optical bends [40] (Fig. 14a). Waveguide junctions, signal splitters and combiners, multimode interferometers, Mach Zehnder interferometers, couplers, and resonators, optimized for footprint or loss depending on the application, are routinely realized (Fig. 14).

C. COUPLED WAVEGUIDES

The optical power of a propagating wave may couple from one waveguide to an adjacent waveguide (Fig. 15). The entire field of the two similar coupled waveguide system may be represented as a superposition of a symmetric and antisymmetric modes traveling at different speeds.

$$\psi(x,z) = \frac{1}{2}e^{\beta_+ z}\left[\psi_+(x) + \psi_-(x)e^{-\frac{z}{L_C}\pi}\right], \tag{11}$$

FIGURE 16. Directional Coupler.

where $L_C = \pi/(\beta_+ - \beta_-)$ is the coupling length, defined as the length at which the entire power couples from one waveguide to another, and is proportional to the exponential gap between the waveguides.

In large-scale dense OPAs, the small distance between adjacent waveguides causes unwanted coupling. The coupling can be reduced by altering the width of adjacent waveguides [10], [39]. It should be noted that the effective refractive index, and hence the propagation velocity, depend on the waveguide width. As such, the phases of signals that propagate trough dissimilar waveguides of the same width are different and may need to be compensated for in the array.

D. DIRECTIONAL COUPLER

Two coupled waveguides can create a directional coupler (Fig. 16) with the input-output relationship given by

$$\begin{bmatrix} E_3 \\ E_4 \end{bmatrix} = \begin{bmatrix} \sqrt{1-k^2} & jk \\ jk & \sqrt{1-k^2} \end{bmatrix} \begin{bmatrix} E_1 \\ E_2 \end{bmatrix}, \tag{12}$$

where coupling factor k depends on the spacing between and lengths of the coupled waveguides.

As a special case, a 3-dB coupler, also known as a quadrature hybrid coupler, is realized when $k = 1/\sqrt{2}$ where

$$\begin{bmatrix} E_3 \\ E_4 \end{bmatrix} = \frac{1}{\sqrt{2}} \begin{bmatrix} 1 & j \\ j & 1 \end{bmatrix} \begin{bmatrix} E_1 \\ E_2 \end{bmatrix}. \tag{13}$$

3-dB coupler are commonly used as power splitters, power dividers, and in Mach-Zehnder interferometers (MZI). 3-dB couplers may be used to share a common antenna for separate receive and transmit paths, although at a fundamental cost of 3 dB loss.

E. MULTI-MODE INTERFEROMETERS

A multi-mode interferometer (MMI) enables splitting or combining the optical power in a compact structure, e.g., a couple of wavelengths in each dimension for a 1:2 MMI. A single-mode waveguide enters a wider multimode region where multiple propagating modes can be supported (Fig. 17). The width of this multi-mode region determines the number of propagating modes. These different propagating modes propagate at different speeds, and as such, add up constructively or destructively at different points along the multi-mode region. The length of the multi-mode region is determined by the number of desired constructive field additions. It should be noted that with the exception of 1:2 MMI, the output phases in a generic 1:N MMIs are not the same.

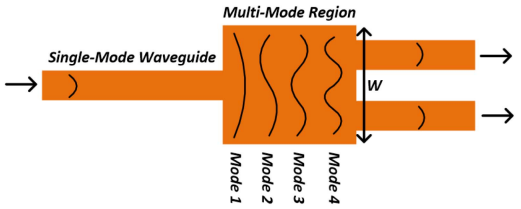

FIGURE 17. Multi-mode interferometer (MMI).

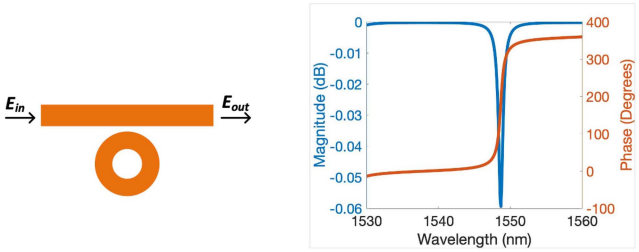

FIGURE 18. Ring resonator coupled to a waveguide along, and a representative all-pass transfer function.

F. MICRORING RESONATORS (MRR)

Microring resonators that are coupled to waveguides (Fig. 18) may be used to realize different transfer functions. For a single microring resonator that is coupled to a single waveguide, the transfer function between the output and input fields may be represented as

$$\frac{E_{out}}{E_{in}} = \frac{\sqrt{1-k^2} - e^{-(\alpha+j\beta)L}}{1-\sqrt{1-k^2}e^{-(\alpha+j\beta)L}}, \tag{14}$$

where k is the coupling factor between the waveguide and resonator (depends on the spacing between the ring and waveguide), $\alpha + j\beta$ is the complex propagation coefficient (α represents loss), and L is the total length of the resonator. The dimensions, determining k and L, may be set to realize high-Q band-stop or all-pass transfer functions. The high-Q all-pass transfer function shows a near constant magnitude versus wavelength while the phase undergoes 360° shift over a small wavelength change (Fig. 18). As such, microring resonators with all-pass transfer functions may be used to realize sensitive low-power variable phase shifters for OPAs. It should be noted that more complex combinations of coupled microring resonators and waveguides may be used to realize a richer set of transfer functions.

G. VARIABLE OPTICAL PHASE SHIFTERS

The optical phase may be adjusted by controlling the propagation speed in the waveguide. Electro-optic and thermo-optic effects are often used to realize variable phase shifters.

The refractive index (n) and loss (α) of silicon depend on the electron and hole free carrier concentrations (ΔN and ΔP respectively) given by (at $\lambda = 1550$ nm and T = 300 K) [32]

$$\begin{cases} \Delta n = 8.8\times10^{-22}\Delta N - 8.5\times10^{-18}\Delta P^{0.8} \\ \Delta\alpha = 8.5\times10^{-18}\Delta N + 6\times10^{-18}\Delta P. \end{cases} \tag{15}$$

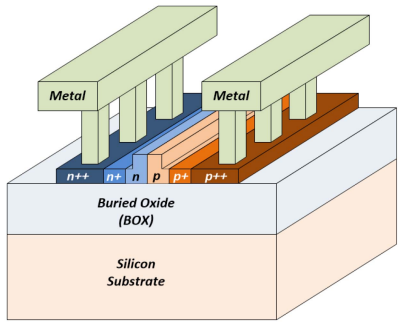

FIGURE 19. Conceptual geometry of an electro-optical variable phase shifter based on changing the carrier concentration in a ridge waveguide.

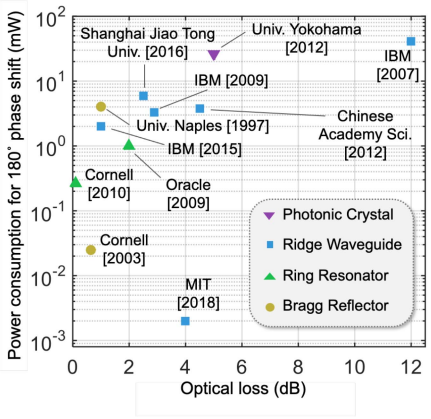

FIGURE 20. Survey of silicon electro-optical phase shifters at 1550 nm.

Ridge silicon waveguides with P and N doings in the ridge region creating a diode are used to create electro-optic variable phase shifters (Fig. 19). These variable phase shifters can be fast and low power especially in the carrier depletion mode when the diode is reverse biased.

As Eqn. (10) suggests, a fundamental tradeoff between phase shift and loss exists in such devices (Fig. 20). This type of phase shifter cannot be realized in Si_3N_4 given the inability to generate free carriers.

The refractive index is a function of temperature. For instance, at $\lambda = 1550$ nm and T = 300 K, the sensitivity of silicon refractive index with temperature dn/dT is $\sim 1.86 \times 10^{-4}$ K^{-1}. Thermo-optic variable phase shifters may be realized by placing a resistive heater next to the waveguide (Fig. 21). The geometry of the waveguide and the placement of the conductive heater can be optimized to realize a compact low-power low-loss thermo-optic phase shifter [39].

Thermo-optic phase shifters are less lossy, more compact, slower, and more power hungry compared with their electro-optic counterparts (Fig. 22). At around $\lambda = 1550$ nm, the sensitivity of refractive index of Si_3N_4 with temperature is around one order of magnitude smaller than that of silicon necessitating a correspondingly larger thermo-optic variable phase shifter size. At visible wavelengths, Si_3N_4 waveguides and thermo-optic phase shifters are commonly used.

Different geometries may be used to enable a more compact or energy-efficient variable phase shifter. For example,

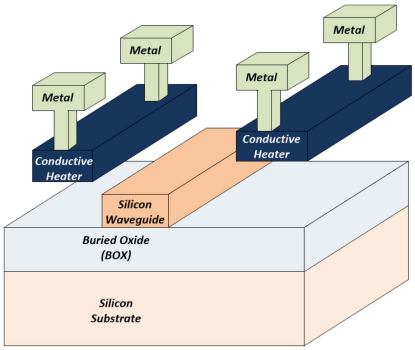

FIGURE 21. Conductive geometry of thermo-optic variable phase shifter.

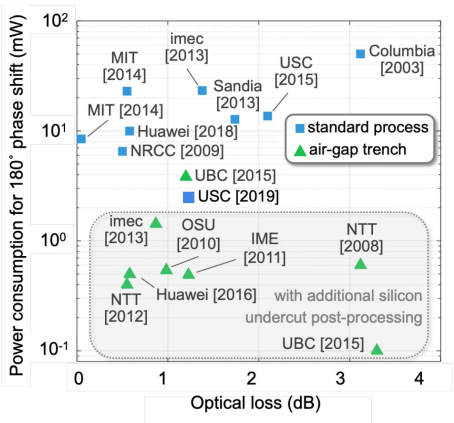

FIGURE 22. Survey of silicon thermo-optical phase shifters at 1550 nm.

microring resonators, properly stabilized using electronic feedback mechanism, may be used to realize low-power compact variable phase shifters (Fig. 18).

H. VARIABLE OPTICAL AMPLITUDE ADJUSTERS

In the absence of gain in today's commercial silicon photonic processes, controlled attenuation is the only way to adjust the amplitude. The electro-optic effect may be used to realize variable attenuators (Eqn. (10)). It is important to note that in this implementation of the variable attenuator, loss and phase shift are related. Alternatively, an interferometer with complementary variable phase shifters in its two arms realize a variable attenuator (Fig. 23) where the output optical fields can be represented as a function of input optical fields as

$$\begin{bmatrix} E_2 \\ 0 \end{bmatrix} = \frac{1}{2}\begin{bmatrix} 1 & j \\ j & 1 \end{bmatrix}\begin{bmatrix} e^{j\theta} & 0 \\ 0 & e^{-j\theta} \end{bmatrix}\begin{bmatrix} 1 & j \\ j & 1 \end{bmatrix}\begin{bmatrix} E_1 \\ 0 \end{bmatrix}, \quad (16)$$

resulting in $E_2 = j\sin\theta \times E_1$.

Naturally, the expected incorporation of gain material in commercial silicon photonic processes [36] enables realization of variable gain amplifiers.

I. ANTENNAS

The optical wave that propagates on planar waveguides can diffract off the surface once impinging on a grating structure. Grating couplers, commonly used to couple the light into

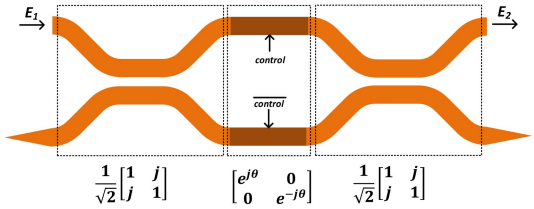

FIGURE 23. Interferometric realization of a variable attenuator.

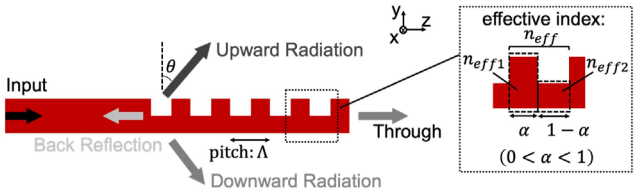

FIGURE 24. Side view of a grating coupler used as an optical antenna.

and outside of the chip, have been the structure of choice to realize optical antennas in phased arrays (Fig. 24). The basic principle of gratings is to create alternating changes in the effective refractive index along a waveguide. This may be done by using different materials (e.g., Si and SiN) or different thicknesses or widths of the same material. The radiation angle is given by

$$\sin\theta = n_{eff} - \frac{\lambda}{\Lambda}, \quad (17)$$

where

$$n_{eff} = \frac{n_{eff1} \times \alpha + n_{eff1} \times (1-\alpha)}{2}. \quad (18)$$

At close to normal radiation angles and for modest values of wavelength change where the n_{eff} remains near constant, the sensitivity of radiation angle to wavelength may be approximated by

$$\frac{d\theta}{d\lambda}|_{\theta\cong 0^\circ} \cong -\frac{n_{eff}}{\lambda}. \quad (19)$$

For instance, for $n_{eff} \cong 3$ and $\lambda = 1500$ nm, $d\theta/d\lambda \cong 0.12^\circ/$ nm which is a typical value achieved in 1D OPAs with wavelength scanning in one dimension (Table 2).

In 2D OPAs, grating couplers are compact, with a few microns in each dimension, ensuring uniformly broad radiation pattern. In 1D OPAs, grating couplers are typically (1) narrow along the array to ensure a wide beam in the ϕ direction as is necessary for interference with beams of other grating couplers, and (2) long perpendicular to the array resulting in a narrow beam in the θ direction. The width and duty cycle of the grating (α) can be adjusted to ensure a constant radiation energy throughout the long grating structure [20]. Overall, the small efficiency of such grating coupler optical antennas, due to a combination of back reflection and radiation through the substrate, is a main source of loss in OPAs.

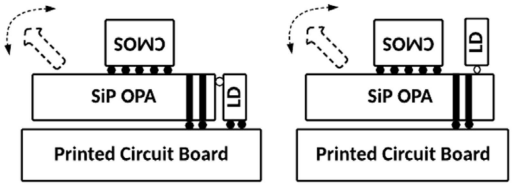

FIGURE 25. Possible hybrid integration of an OPA.

J. LASERS

In many OPA demonstrations, the light from an off-chip laser is coupled to the chip using an edge or a grating coupler. There are a few examples of reported OPAs with electrically or optically pumped lasers on the chip [13], [37]. It is possible that future OPAs will leverage recent advancements in commercial heterogenous integration of lasers on SiP chips [36].

K. ELECTRONICS

Variable optical phase shifters and amplitude adjusters must be controlled by appropriate electronic circuitry. The size and power consumption of electronic circuits, including digital to analog converters and drivers, should be very small. Architectural innovations, such as time multiplexing and pulse-width modulation for the slow thermo-optical variable phase shifters and amplitude adjusters, may also be exploited [9], [23].

Large-scale optical phased arrays require a tight photonic-electronic integration either monolithically [7], [23] or hybrid [17], *e.g.*, stacked dies with thru-silicon vias (Fig. 25).

VI. CONCLUSION

The architectural choice for an OPA depends on the application. For instance, in automotive lidars with limited required field-of-view in the vertical direction, if forming and steering a single beam is sufficient, a 1D array with wavelength-based beam scanning in the other direction may be sufficient. On the other hand, a 3D imager or projection display with large fields-of-view in both directions may require a 2D array. Large-scale monolithic 1D OPAs with subwavelength antenna pitch, mostly realized as a silicon photonic integrated circuit at the 1550 nm wavelength, with custom CMOS circuits for control, have been reported [18]–[20].

Large-scale 2D OPAs with near half-wavelength antenna pitch, and independent control of the phase and amplitude of each antenna, remains an open research challenge. Subwavelength optical components such as antennas, couplers, and variable phase shifters are the key enablers of such a scheme. Photonic integrated circuits capable of realizing optical components at multiple layers (3D PICs) would also benefit realization of such large-scale 2D phased arrays.

The unwanted coupling (optical, thermal, electrical) between various components of a compact large-scale phased array affects the performance. Predicting, reducing, or otherwise mitigation the effect of such coupling is an important research problem.

Nearly all reported optical phased arrays are calibrated in the lab using benchtop optics and cameras, while the few on-chip calibration schemes are used to maintain the established operation of the already-calibrated array over time in light of environmental variations. Commercial deployment of optical phased arrays would require low-cost methods for test and calibration in the factory as well as during operation – both remain open research problems.

With a few exceptions [27]–[29], most reported OPAs operate at the 1550 nm wavelength. Optical phased arrays at the visible wavelengths enable interesting applications such as holographic projection [30] and optical neural probes [31], whereas OPAs operating at longer wavelengths might be preferred for longer-range free-space optical communication, imaging, and sensing. Optical phased arrays that cover a broad range of wavelengths and can possibly operate at multiple wavelengths simultaneously, e.g., for independent beam-steering of different wavelengths, would enable a host of new interesting applications in communication, sensing, and imaging.

Optical phased arrays with element- or subarray-level digitization and processing capability is another interesting are of future research. Such *digital optical phased arrays* can enable concurrent multi-beam formation and multi-input multi-output (MIMO) schemes.

Design and optimization of OPAs is currently a tedious process that involves design and optimization of individual components and a nontrivial device placement and optical routing network that minimizes the loss and unwanted coupling. Computer aided design tools that can automate some aspects of the design and optimization are worthy research topics.

ACKNOWLEDGMENT

The material of this paper is influenced by the research conducted by Hooman Abediasl, SungWon Chung, and Makoto Nakai while at USC. Figures 20 and 22 were prepared by SungWon Chung.

REFERENCES

[1] K. Braun, *Electrical Oscillations and Wireless Telegraphy*, Nobel Lecture, Nobel Found., Stockholm, Sweden, Dec. 1909.
[2] G. Moore, "Cramming more components onto integrated circuits," *Electronics*, vol. 38, no. 8, pp. 114–117, Apr. 1965.
[3] F. Sterzer, "Phased array light deflecting system," U.S. Patent 3 331 651 A, 1967.
[4] W. Bridges *et al.*, "Coherent optical adaptive techniques," *Appl. Opt.*, vol. 13, no. 3, pp. 291–300, 1974.
[5] T. Komljenovic, R. Helkey, L. Coldren, and J. Bowers, "Sparse aperiodic arrays for optical beam forming and LIDAR," *Opt. Exp.*, vol. 25, no. 3, pp. 2511–2528, 2017.
[6] J. Sun, E. Timurdogan, A. Yaacobi, E. S. Hosseini, and M. R. Watts, "Large-scale nanophotonic phased array," *Nature*, vol. 493, no. 7431, pp. 195–199, 2013.
[7] H. Abediasl and H. Hashemi, "Monolithic optical phased-array transceiver in a standard SOI CMOS process," *Opt. Exp.*, vol. 23, no. 5, pp. 6509–6519, 2015.
[8] F. Aflatouni, B. Abiri, A. Rekhi, and A. Hajimiri, "Nanophotonic projection system," *Opt. Exp.*, vol. 23, no. 16, pp. 21012–21022, 2015.

[9] R. Fatemi, A. Khachaturian, and A. Hajimiri, "A nonuniform sparse 2-D large-FOV optical phased array with a low-power PWM drive," *IEEE J. Solid-State Circuits*, vol. 54, no. 5, pp. 1200–1215, May 2019, doi: 10.1109/JSSC.2019.2896767.
[10] C. T. Phare, M. C. Shin, J. Sharma, S. Ahasan, H. Krishnaswamy, and M. Lipson, "Silicon optical phased array with grating lobe-free beam formation over 180 degree field of view," in *Proc. Conf. Lasers Electro-Opt. (CLEO)*, 2018, pp. 1–2.
[11] J. K. Doylend, M. J. R. Heck, J. T. Bovington, J. D. Peters, L. A. Coldren, and J. E. Bowers, "Two-dimensional free-space beam steering with an optical phased array on silicon-on-insulator," *Opt. Exp.*, vol. 19, no. 22, pp. 21595–21604, 2011.
[12] D. Kwong *et al.*, "On-chip silicon optical phased array for two-dimensional beam steering," *Opt. Lett.*, vol. 39, no. 4, pp. 941–944, 2014.
[13] J. C. Hulme *et al.*, "Fully integrated hybrid silicon two dimensional beam scanner," *Opt. Exp.*, vol. 23, no. 5, pp. 5861–5874, 2015.
[14] D. Hutchison *et al.*, "High-resolution aliasing-free optical beam steering," *Optica*, vol. 3, no. 8, pp. 887–890, 2016.
[15] S. A. Miller *et al.*, "512-element actively steered silicon phased array for low-power LIDAR," in *Proc. Conf. Lasers Electro-Opt.*, 2018, Art. no. JTh5C.2.
[16] C. V. Poulton, M. J. Byrd, E. Timurdogan, P. Russo, D. Vermeulen, and M. R. Watts, "Optical phased arrays for integrated beam steering," in *Proc. IEEE 15th Int. Conf. Group IV Photon. (GFP)*, 2018, pp. 1–2, doi: 10.1109/GROUP4.2018.8478729.
[17] T. Kim *et al.*, "A single-chip optical phased array in a wafer-scale silicon photonics/CMOS 3D-integration platform," *IEEE J. Solid-State Circuits*, vol. 54, no. 11, pp. 3061–3074, Nov. 2019, doi: 10.1109/JSSC.2019.2934601.
[18] Y. Zhang *et al.*, "Sub-wavelength-pitch silicon-photonic optical phased array for large field-of-regard coherent optical beam steering," *Opt. Exp.*, vol. 27, no. 3, pp. 1929–1940, 2019.
[19] C. V. Poulton, M. J. Byrd, B. Moss, E. Timurdogan, R. Millman, and M. R. Watts, "8192-element optical phased array with 100° steering range and flip-chip CMOS," in *Conf. Lasers Electro-Opt. OSA Tech. Dig.*, 2020, Art. no. JTh4A.3.
[20] S. Chung, M. Nakai, S. Idres, Y. Ni, and H. Hashemi, "Optical phased array FMCW lidar with on-chip calibration," in *IEEE Int. Solid-State Circuits Conf. Dig. Tech. Papers*, Feb. 2021, pp. 286–287.
[21] K. Van Acoleyen, W. Bogaerts, J. Jágerská, N. Le Thomas, R. Houdré, and R. Baets, "Off-chip beam steering with a one-dimensional optical phased array on silicon-on-insulator," *Opt. Lett.*, vol. 34, no. 9, pp. 1477–1479, 2009.
[22] C. V. Poulton, A. Yaacobi, Z. Su, M. J. Byrd, and M. R. Watts, "Optical phased array with small spot size, high steering range and grouped cascaded phase shifters," in *Adv. Photon. (IPR, NOMA, Sensors, Networks, SPPCom, SOF) OSA Tech. Dig.*, 2016, Art. no. IW1B.2.
[23] S. Chung, H. Abediasl, and H. Hashemi, "A monolithically integrated large-scale optical phased array in silicon-on-insulator CMOS," *IEEE J. Solid-State Circuits*, vol. 53, no. 1, pp. 275–296, Jan. 2018.
[24] R. Fatemi, B. Abiri, A. Khachaturian, and A. Hajimiri, "High sensitivity active flat optics optical phased array receiver with a two-dimensional aperture," *Opt. Exp.*, vol. 26, no. 23, pp. 29983–29999, 2018.
[25] C. Rogers *et al.*, "A universal 3D imaging sensor on a silicon photonics platform," *Nature*, vol. 590, pp. 256–261, Feb. 2021.
[26] J. Shim *et al.*, "On-chip monitoring of far-field patterns using a planar diffractor in a silicon-based optical phased array," *Opt. Lett.*, vol. 45, no. 21, pp. 6058–6061, 2020.
[27] M. Shin *et al.*, "Chip-scale blue light phased array," *Opt. Lett.*, vol. 45, no. 7, pp. 1934–1937, Apr. 2020.
[28] J. Midkiff, K. Yoo, J. Shin, H. Dalir, M. Teimourpour, and R. Chen, "Optical phased array beam steering in the mid-infrared on an InP-based platform," *Optica*, vol. 7, no. 11, pp. 1544–1547, 2020.
[29] H. Wang *et al.*, "Broadband silicon nitride nanophotonic phased arrays for wide-angle beam steering," *Opt. Lett.*, vol. 46, no. 2, pp. 286–289, 2021.
[30] J. Notaros, M. Raval, M. Notaros, and M. R. Watts, "Integrated-phased-array-based visible-light near-eye holographic projector," in *Conf. Lasers Electro-Opt. OSA Tech. Dig.*, 2019, Art. no. STu3O.4.
[31] L. Moreaux *et al.*, "Integrated neurophotonics: Toward dense volumetric interrogation of brain circuit activity—At depth and in real time," *Neuron*, vol. 108, no. 1, pp. 66–92, 2020.
[32] R. Soref and B. Bennett, "Electrooptical effects in silicon," *IEEE J. Quantum Electron.*, vol. QE-23, no. 1, pp. 123–129, Jan. 1987.
[33] R. Soref, "The past, present, and future of silicon photonics," *IEEE J. Sel. Topics Quantum Electron.*, vol. 12, no. 6, pp. 1678–1687, Nov./Dec. 2006, doi: 10.1109/JSTQE.2006.883151.
[34] B. Jalali and S. Fathpour, "Silicon photonics," *J. Lightw. Technol.*, vol. 24, no. 12, pp. 4600–4615, Dec. 2006, doi: 10.1109/JLT.2006.885782.
[35] J. Notaros, C. Poulton, M. Raval, and M. Watts, "Near-field-focusing integrated optical phased arrays," *J. Lightw. Technol.*, vol. 36, pp. 5912–5920, Dec. 15, 2018.
[36] G. Keeler. "Lasers for Universal Microscale Optical Systems (LUMOS)." Accessed: Sep. 1, 2020. [Online]. Available: https://www.darpa.mil/program/lasers-for-universal-microscale-optical-systems
[37] J. Notaros *et al.*, "CMOS-compatible optical phased array powered by a monolithically-integrated erbium laser," *J. Lightw. Technol.*, vol. 37, pp. 5982–5987, Dec. 15, 2019.
[38] T. Komljenovic and P. Pintus, "On-chip calibration and control of optical phased arrays," *Opt. Exp.*, vol. 26, no. 3, pp. 3199–3210, 2018.
[39] S. Chung, M. Nakai, and H. Hashemi, "Low-power thermo-optic silicon modulator for large-scale photonic integrated systems," *Opt. Exp.*, vol. 27, no. 9, pp. 13430–13459, 2019.
[40] M. Nakai, T. Nomura, S. Chung, and H. Hashemi, "Geometric loss reduction in tight bent waveguides for silicon photonics," in *Proc. Conf. Lasers Electro-Opt. (CLEO)*, May 2018, pp. 1–2.

HOSSEIN HASHEMI (Fellow, IEEE) received the B.S. and M.S. degrees in electronics engineering from the Sharif University of Technology, Tehran, Iran, in 1997 and 1999, respectively, and the M.S. and Ph.D. degrees in electrical engineering from the California Institute of Technology, Pasadena, CA, USA, in 2001 and 2003, respectively.

He is currently a Professor of Electrical and Computer Engineering, the Ming Hsieh Faculty Fellow, and the Co-Director of the Ming Hsieh Institute, University of Southern California, Los Angeles, CA, USA. He is a Co-Editor of the books *Millimeter-Wave Silicon Technology: 60 GHz and Beyond* (Springer, 2008) and *mm-Wave Silicon Power Amplifiers and Transmitters* (Cambridge University Press, 2016). His research interests include electronic and photonic integrated circuits and systems.

Prof. Hashemi was a recipient of the 2016 Nokia Bell Labs Prize, the 2015 IEEE Microwave Theory and Techniques Society Outstanding Young Engineer Award, the 2008 Defense Advanced Research Projects Agency Young Faculty Award, the National Science Foundation CAREER Award, and the USC Viterbi School of Engineering Junior Faculty Research Award in 2008. He was recognized as a Distinguished Scholar for the Outstanding Achievement in Advancement of Engineering by the Association of Professors and Scholars of Iranian Heritage in 2011. He was a co-recipient of the 2004 IEEE JOURNAL OF SOLID-STATE CIRCUITS Best Paper Award for A Fully Integrated 24 GHz 8-Element Phased-Array Receiver in Silicon and the 2007 IEEE International Solid-State Circuits Conference Lewis Winner Award for Outstanding Paper for A Fully Integrated 24 GHz 4-Channel Phased-Array Transceiver in 0.13-μm CMOS Based on a Variable Phase Ring Oscillator and PLL Architecture. He was an Associate Editor of the IEEE TRANSACTIONS ON CIRCUITS AND SYSTEMS—PART I: REGULAR PAPERS from 2006 to 2007, the IEEE TRANSACTIONS ON CIRCUITS AND SYSTEMS—PART II: EXPRESS BRIEFS from 2004 to 2005, and the IEEE JOURNAL OF SOLID-STATE CIRCUITS from 2013 to 2019. He was a Guest Editor of the IEEE JOURNAL OF SOLID-STATE CIRCUITS in 2013. He is currently an Associate Editor for the IEEE OPEN JOURNAL OF THE SOLID-STATE CIRCUITS SOCIETY. He was a Distinguished Lecturer of the IEEE Solid-State Circuits Society from 2013 to 2014. He was a member of the Technical Program Committee of the IEEE International Solid-State Circuits Conference from 2011 to 2015, the IEEE Radio frequency Integrated Circuits Symposium from 2011 to 2019, and the IEEE Compound Semiconductor Integrated Circuits Symposium from 2010 to 2014.